Burner Rig With an Unattached Duct for Evaluating the Erosion Resistance of Thermal Barrier Coatings

Robert A. Miller, Maria A. Kuczmarski, and Dongming Zhu
Glenn Research Center, Cleveland, Ohio

NASA STI Program . . . in Profile

Since its founding, NASA has been dedicated to the advancement of aeronautics and space science. The NASA Scientific and Technical Information (STI) program plays a key part in helping NASA maintain this important role.

The NASA STI Program operates under the auspices of the Agency Chief Information Officer. It collects, organizes, provides for archiving, and disseminates NASA's STI. The NASA STI program provides access to the NASA Aeronautics and Space Database and its public interface, the NASA Technical Reports Server, thus providing one of the largest collections of aeronautical and space science STI in the world. Results are published in both non-NASA channels and by NASA in the NASA STI Report Series, which includes the following report types:

- TECHNICAL PUBLICATION. Reports of completed research or a major significant phase of research that present the results of NASA programs and include extensive data or theoretical analysis. Includes compilations of significant scientific and technical data and information deemed to be of continuing reference value. NASA counterpart of peer-reviewed formal professional papers but has less stringent limitations on manuscript length and extent of graphic presentations.

- TECHNICAL MEMORANDUM. Scientific and technical findings that are preliminary or of specialized interest, e.g., quick release reports, working papers, and bibliographies that contain minimal annotation. Does not contain extensive analysis.

- CONTRACTOR REPORT. Scientific and technical findings by NASA-sponsored contractors and grantees.

- CONFERENCE PUBLICATION. Collected papers from scientific and technical conferences, symposia, seminars, or other meetings sponsored or cosponsored by NASA.

- SPECIAL PUBLICATION. Scientific, technical, or historical information from NASA programs, projects, and missions, often concerned with subjects having substantial public interest.

- TECHNICAL TRANSLATION. English-language translations of foreign scientific and technical material pertinent to NASA's mission.

Specialized services also include creating custom thesauri, building customized databases, organizing and publishing research results.

For more information about the NASA STI program, see the following:

- Access the NASA STI program home page at *http://www.sti.nasa.gov*

- E-mail your question via the Internet to *help@ sti.nasa.gov*

- Fax your question to the NASA STI Help Desk at 443–757–5803

- Telephone the NASA STI Help Desk at 443–757–5802

- Write to:
  NASA Center for AeroSpace Information (CASI)
  7115 Standard Drive
  Hanover, MD 21076–1320

Burner Rig With an Unattached Duct for Evaluating the Erosion Resistance of Thermal Barrier Coatings

Robert A. Miller, Maria A. Kuczmarski, and Dongming Zhu
Glenn Research Center, Cleveland, Ohio

Level of Review: This material has been technically reviewed by technical management.

Available from

Burner Rig With an Unattached Duct for Evaluating the Erosion Resistance of Thermal Barrier Coatings

Robert A. Miller, Maria A. Kuczmarski, and Dongming Zhu
National Aeronautics and Space Administration
Glenn Research Center
Cleveland, Ohio 44135

Abstract

Extensive computational fluid dynamics (CFD) modeling backed by experimental observation has demonstrated the feasibility of using an unattached duct to increase the velocity and spatial spread of erodent particles exiting from a burner rig. It was shown that gas velocity and temperature are mostly retained if the inner diameter of the unattached duct equaled the exit diameter of the burner rig nozzle. For particles having a mean diameter of 550 μm, the modeled velocity attained at a distance 2.0 in. (50.8 mm) beyond the exit of a 12 in. (305 mm) long duct was approximately twice as large as the velocity the same distance from the nozzle when the duct was not present. For finer particles, the relative enhancement was somewhat less—approximately 1.5 times greater. CFD modeling was also used to guide the construction of a device for slowing down the velocity of the particles being injected into the burner rig. This device used a simple 45° fitting to slow the particle velocity in the feed line from 20 m/s, which is in the range needed to convey the particles, to about 3 m/s just as they are injected into the burner. This lower injection velocity would lessen the severity of the collision of large particles with the wall of the burner liner opposite the injection port, thereby reducing potential damage to the burner liner by high-velocity particles.

Introduction

Projected performance goals for rotorcraft engines require a 30 percent efficiency improvement over the next decade and further improvements in subsequent decades (Ref. 1). Performance and efficiency improvements generally require higher gas temperatures, higher pressures, and lower cooling air flows. This means that future thermal barrier-coated turbine section components will have to operate at increased surface temperatures, requiring the thermal barrier coatings (TBCs) to be more resistant to high-temperature sintering. In addition, TBC thermal conductivity will have to be reduced in order to minimize coating thickness. However, the reduced conductivity and improved sintering resistance of turbine blade coatings must not come at the expense of reduced erosion resistance. TBC compositions with combined high toughness, erosion resistance, and low thermal conductivity have to be used for turbine component applications in the harsher environments within the advanced rotorcraft engines. For example, it is known that zirconia-yttria-gadolinia-ytterbia TBCs having compositions from the cubic phase field have lower conductivity and reduced erosion resistance compared with tougher compositions taken from the tetragonal phase field (Refs. 2 and 3). Although the cubic compositions would be favored for combustor applications where erosion is not a concern, they would likely be ruled out in favor of tetragonal compositions for high-pressure turbine blade applications. For the same reason, another class of lower conductivity zirconia-based TBCs, known as pyrochlores, may not be the best choice for high-pressure turbine blades from the erosion standpoint (Ref. 3). Therefore, tetragonal phase, low conductivity/sinter resistant TBCs must be considered for future advanced rotorcraft turbine blade applications.

Solid particles interacting with TBCs may remove coating material by either of two types of processes, depending on particle size. Smaller particles having diameters of tens of microns cause erosion, which is characteristically gradual. Larger particles having diameters of hundreds of microns cause impact damage, which may be sudden. Coating damage that does not result in removal of the

coating can also occur. Prior to sudden failure, large particles can cause coating densification (Ref. 4). In addition, under certain combinations of particle compositions and temperatures, fine particles can melt, causing damage by corrosion (Ref. 5). Since this study will concentrate on damage resulting from particle impacts, the effects of corrosion will not be discussed further.

TBC removal by erosion and impact damage is especially likely at the leading and trailing edges of the turbine blades (Ref. 6). Rotorcraft engines are subject to greater loading of injected particulate matter than other types of turbine engines because rotorcraft may operate at relatively low altitudes, take off and land from less improved landing sites, and their operation involves hovering that may stir up considerable amounts of particulates. While these factors can be especially true for certain military missions, they also apply for commercial missions that are the primary focus of NASA. Particle separators can remove large ingested particles, but particles with diameters on the order of tens of microns can reach the turbine section, especially during periods of heavy loading. Travel through the compressor tends to reduce particle size further (Refs. 7 and 8), insuring that ingested particulate sizes are in the range likely to causes erosion. However, particles of carbon, zirconia, or other debris hundreds of microns in diameter or larger may shed from the combustor and cause impact damage to the turbine blade TBC (Refs. 9 and 10). Therefore, future TBCs must be resistant to both erosion and impact resistance.

Effective and affordable laboratory methods for evaluating and understanding erosion and impact resistance of TBCs are needed. Erosion rigs used for TBC research have tended to be one of two types. In one type, erodent particulates are injected into a burner rig and accelerated through an exhaust nozzle towards a test specimen, with the acceleration continuing for a short distance afterwards in the potential core of the flame. Examples of burner rig-based erosion rigs are a rig at General Electric (Ref. 11), a former rig at NASA (Ref. 12), and the current rig at NASA (Ref. 3). Alternatively, erosion rigs are combustion-driven ducted rigs where the acceleration occurs throughout the length of a duct. Examples of the latter type of rig are the wind-tunnel rig at the University of Cincinnati (Refs. 13 and 14) and the ducted rig at Cranfield (Ref. 4). Erodent particles can be accelerated to higher velocities in ducted rigs than in burner rigs, but burner rigs are generally simpler and capable of achieving higher temperatures. Placing a short duct after a burner rig nozzle exit and before a test specimen could combine positive features of both by allowing further acceleration of the ingested particles without losing excessive heat. A photograph of the unducted burner rig at NASA, adapted from Figure 1 of Reference 3, is shown in Figure 1. The burner in the lower portion of this figure has pivoted to the cooling position away from the specimen. The specimen in this portion of the figure is 50.8 mm in diameter and it has been spot-welded to the fixture. A 25.4 mm specimen held in a spring-loaded clam-shell fixture is shown in the insert. This specimen is being heated by the burner rig flame that is operated using jet fuel and preheated air. Erodent powder, usually alumina grit, is injected into the burner using a feeder of the type used in plasma spraying. Alumina is chosen because it is readily available and it produces damage in rig tests that matches the damage seen in engine experience (Ref. 11).

The current rig at the NASA Glenn Research Center is a modified jet-fuel/preheated air fired burner rig typically referred to as a "Mach 0.3 burner rig." It has been modified for operation up to Mach 1 by increasing the air flow and switching from a nozzle that was 1.00 in. (25.4 mm) in diameter to one that is 0.75 in. (19.05 mm) in diameter using design concepts suggested for ASTM flow nozzles (Ref. 15). This rig has been described elsewhere for erosion testing involving particles tens of microns in diameter (Ref. 3) and is quite similar to a former rig at NASA described by Handschuh (Ref. 12). Although this rig accelerates the small particles to adequately high velocities, the burner rig approach does not accelerate large particles to high velocities (Ref. 11). Unfortunately, the NASA burner rig does not readily lend itself to attaching a duct for increasing particle velocities because specimen temperature cycling is accomplished by rather forceful pivoting of the burner using pneumatic actuators. This pivoting, even if redesigned for more gentle motion, would soon cause misalignment of a duct.
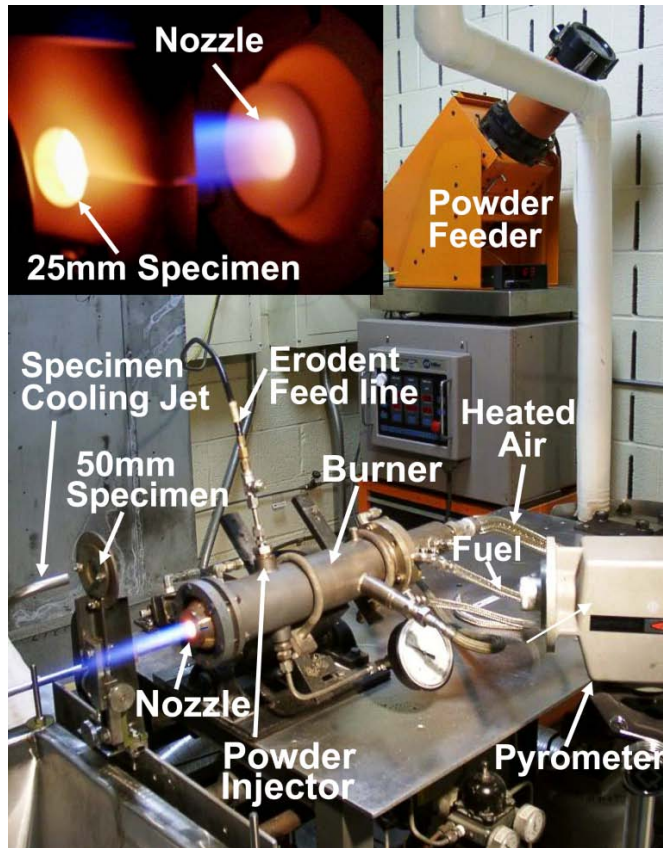
Figure 1.—Photograph of the unducted erosion burner rig at NASA.

The goal of this study is to determine whether a new erosion rig design, having an unattached stationary duct and a pivoting burner rig, would be feasible for conducting erosion burner rig exposure of advanced coatings. This approach would allow the burner rig to pivot in front of the unattached duct in the heating position and away from the duct in the cooling position. This paper presents the results of extensive CFD modeling backed by laboratory experiments that demonstrate the feasibility of such a design, along with an experimental examination of the effect of such a duct on the behavior of small particles.

Model Description

The computational fluid dynamics code FLUENT (Ref. 1) was used to model the experimental apparatus. The code uses a finite volume method to discretize the continuity, momentum, and energy equations. An axisymmetric model was used; various regions and boundary conditions are shown on Figure 2. In this figure, the dimensions represent cases having the 12 in. (305 mm) long, 0.75 in. (19.05 mm) diameter duct. Other duct diameters and lengths, as well as cases having no duct, were modeled and will be discussed. The spacing between the nozzle exit and the duct entrance was set to 0.50 in. (12.7 mm). For the cases examined in this paper, gas enters at the pressure inlet on the far left of the drawing, passes through the nozzle and exits at the pressure outlet at the far right. A relatively small amount of air enters though the two pressure inlets at the top and left side of the box that bounds the region of the model after the nozzle exit. The air entering through the pressure inlets in the box results from air that aspirates into the gas jet.
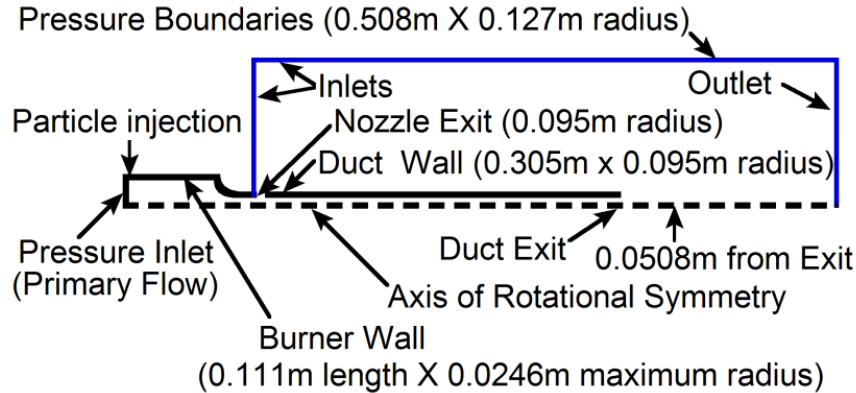
Figure 2.—Schematic drawing of burner rig and duct as used for the CFD model. The same geometry was used for all cases, except that the length and vertical position (radius) of the duct was varied.

A standard k-epsilon turbulence model with the C1-epsilon changed from the standard value of 1.44 to 1.56 was used as a starting point for a numerical study of this apparatus because of the successful use of this turbulence model by Senesh and Babu (Ref. 16) to describe the potential core and other characteristics of similar jets. Strictly speaking, this model is only applicable for fully-developed turbulent flow. The range of flows used in this study yielded Mach numbers at the nozzle exit from 0.3 to 1.0. Reynolds numbers at these Mach numbers were about 8,300 and 21,000, respectively, which is in the range for turbulent flow. However it is likely fully developed turbulent flow is not actually established in this problem because of the relatively short axial length. Nonetheless, because the model with the modified C1 constant predicted a potential core having a length matching that observed experimentally—both in our case and with the work of Senesh and Babu—it was felt that the k-epsilon model would be fully adequate for the needs of this study. Standard wall functions were used and viscous heating was enabled. The discrete phase model was activated to allow solid particles to be injected into the gas flow and their paths tracked. These particles were allowed to interact with the gas phase. A spherical particle drag law from Morsi and Alexander (Ref. 17) was used:

$$C_d = a_1 + \frac{a_2}{\text{Re}} + \frac{a_3}{(\text{Re})^2} \tag{1}$$

where C_d is the drag coefficient, Re is the Reynolds number, and the values of the constant are described in Morsi and Alexander. This drag law was further modified using a high Mach number drag law (Ref. 18). This modification affects the drag law for relative Mach numbers greater than 0.4.

Injections were defined as inert alumina particles released across the surface of the particle inlet. Three particle injection velocities were employed for each case—a minimum, a maximum, and a velocity midway between the two.

A second-order upwind scheme was used for both the momentum and energy equations, with an under-relaxation factor set to 0.3 for the momentum equation and 1 for the energy equation. The convergence criteria for the solutions were defined as scaled residuals below 1×10^{-5} for the momentum equation, 1×10^{-6} for the energy equation, and 1×10^{-3} for both the turbulent kinetic energy and dissipation rate. Decreasing these values did not result in a change in the model predictions.

The sensitivity of the results to the grid density was studied using three different grid densities based on the number of cells used across the nozzle. A non-uniform grid was used over parts of the model to minimize the total number of computational cells. The maximum aspect ratio for the cells was 5:1. Using 10 cells across the nozzle yielded 15,393 total cells in the computational domain, 15 cells across the nozzle yielded 34,251 total cells, and 20 cells across the nozzle yielded 61,257 total cells. Comparisons were made

among the grids for both temperature and velocity magnitude at a number of points that spanned the radius of the nozzle and a distance of 0.1016 m from the nozzle exit. Comparisons of temperature among the grids at identical points yielded differences of generally less than 1 percent, with the maximum difference being 3 percent. Similar comparisons of velocity magnitude yielded differences generally less than 2 percent, with the maximum difference being 6 percent. This shows that the grid with 15,393 total cells is sufficient to achieve grid-independent results. This grid was used for the rest of the study.

Values for normal and tangential restitution coefficients, which are required by FLUENT, were based on room temperature measurements of the velocity- and directional-restitution coefficients reported in the literature (Refs. 7 and 19). The literature values show that the angle of impact of particles colliding with a wall is very similar to the angle of reflection. For the purposes of this paper, it is sufficient to allow the angle of incidence to equal the angle of reflection. After making this simplifying assumption, the normal and tangential restitution coefficients must be equal to each other and their value will be equal to the velocity restitution coefficient, where the velocity restitution coefficient is the ratio of the particle velocity after striking a surface to the velocity before the collision. At least for the case of smaller particles in the range that causes erosion damage, the value reported for the velocity restitution coefficient appears to be close to 0.5 at essentially all collision angles. A lack of angular dependence may imply a balanced combination of the effects of friction (whose effect is strongest at lower angles) and plastic deformation (whose effect is strongest at higher angles). Friction is related to surface roughness and particle size. Plasticity may be related to the hardness of the particle and the surface with which it collides.

The velocity restitution coefficient, measured at room temperature for large particles, is near 1.0 (near elastic) for low angle collisions falling off at higher angles (Ref. 19). The data from Swar (Ref. 19) was approximated by two polynomials. One segment of the polynomial gave a restitution coefficient between 0.96 and 0.97 between 0° and 15°, and the other segment allowed the restitution coefficient to drop to 0.25 at 90°. This will be referred to as "near-elastic-forward restitution" in the paper. For our experimental case of a high temperature mullite duct, the surface may be relatively soft, which could lower the forward restitution coefficient. Because of the uncertainty, two types of velocity restitution coefficients were used for the large particle calculations. For one group, the particle dynamics were calculated using restitution coefficients that matched the results reported; another set of cases used the value of 0.5 at all angles. The directional restitution coefficient for all cases was simply allowed to equal 1.0, making the angle of reflection equal to the angle of incidence.

Modeling Results

Modeling of Unattached Ducted Rig

Extensive CFD modeling was conducted to investigate the new unattached ducted rig concept. Initial runs focused on the behavior of the gas phase when the rig was operated at Mach 0.5. Gas temperature and velocity plots are shown in Figure 3. For all cases, the distance between the nozzle exit and the duct entrance was set to 0.5 in. (12.7 mm). The case with the largest duct diameter—1.94 in. (49.3 mm)— behaved essentially the same as a rig not having a duct. Practically speaking, it could be viewed as a windscreen rather than a duct. The figures for the corresponding unducted case are not shown because they are visually nearly identical to this case. Decreasing duct diameter to 1.0 in. (25.4 mm) showed a similarly short potential core (as approximated by the red-colored region of the figure). Decreasing the duct further to equal the duct diameter of 0.75 in. (1.905 mm) resulted in a flame having an extended potential core whose length was several inches longer than the length of the 4.5 in. (44.5 mm) duct. Extending the duct length to 12 in. (305 mm), the approximate maximum length available in the test cell, produced a potential core several inches longer than the length of the longer duct.
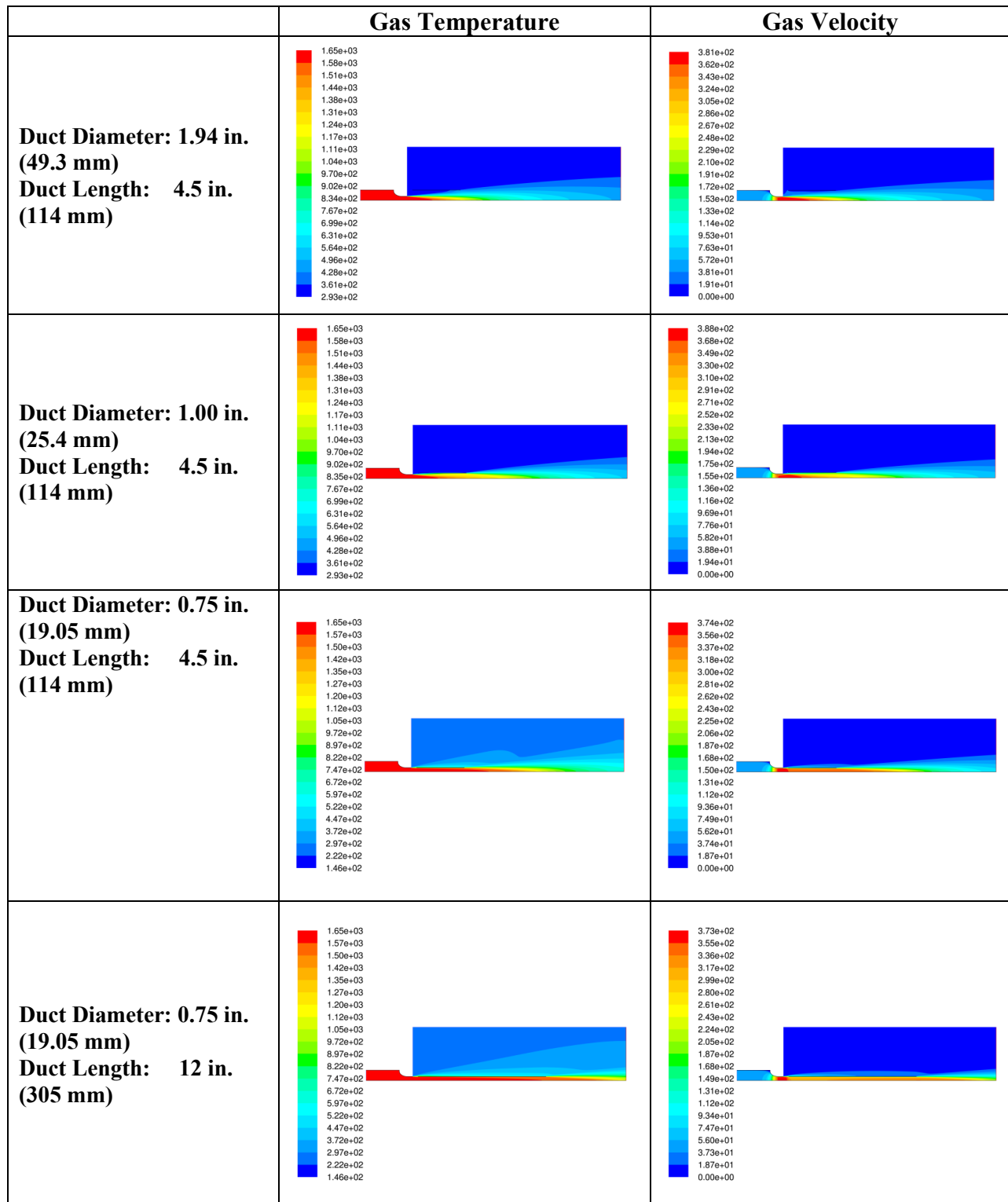
	Gas Temperature	Gas Velocity
Duct Diameter: 1.94 in. (49.3 mm) **Duct Length: 4.5 in. (114 mm)**		
Duct Diameter: 1.00 in. (25.4 mm) **Duct Length: 4.5 in. (114 mm)**		
Duct Diameter: 0.75 in. (19.05 mm) **Duct Length: 4.5 in. (114 mm)**		
Duct Diameter: 0.75 in. (19.05 mm) **Duct Length: 12 in. (305 mm)**		

Figure 3.—Gas total temperature and velocity magnitude plots for a burner rig operated at 2500 °F (1371 °C, 1644 K) and Mach 0.5. Showing duct diameter of 19.05 mm and length of 114 and 305 mm. Geometric dimensions of the 12 in. (305 mm) case are given in Figure 2.
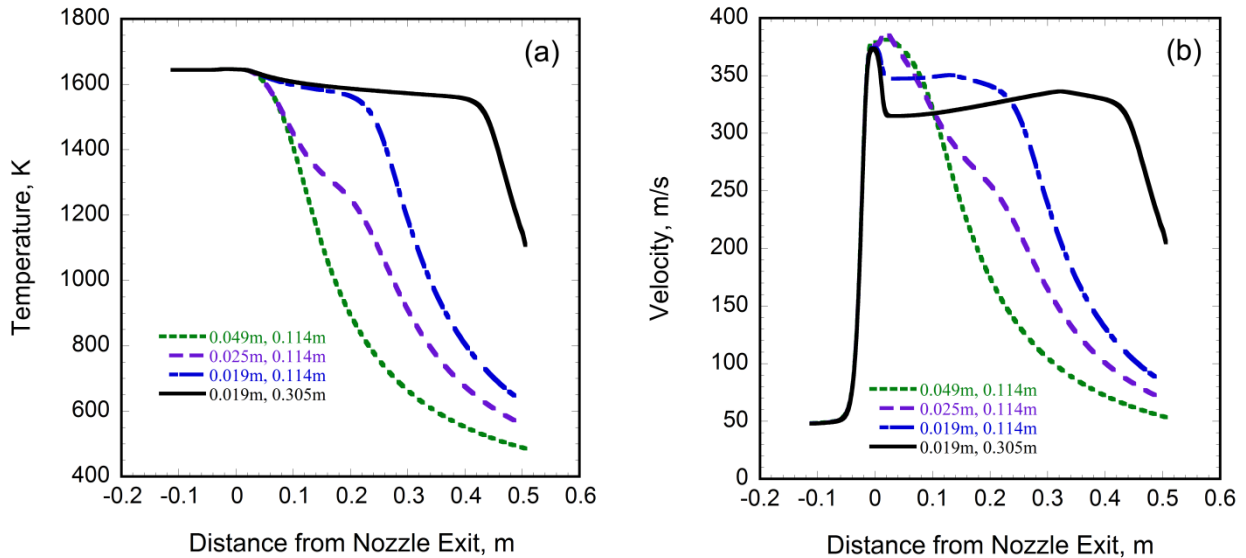
Figure 4.—Centerline (a) total temperatures and (b) velocity magnitudes corresponding to Figure 3.

The centerline total temperatures and velocities taken from the text data corresponding to the above plots for the four ducts are shown in Figures 4(a) and (b), respectively. Note that for the 1.94 in. (49.3 mm) diameter duct and the 1.00 in. (25.4 mm) duct, the total temperature of the gas falls off quickly after a few inches from the nozzle (i.e., it quickly drops off after exiting the relatively short potential core of the jet). For the 4.5 in. (49.3 mm) long, 0.75 in. (1.905 mm) diameter duct, the temperature is largely maintained throughout the length of the duct and a few inches beyond. For the 12 in. (305 mm) long, 0.75 in. (1.905 mm) diameter duct, the temperature is again maintained up to a few inches beyond duct exit. Gas velocity falls off more quickly initially but then recovers and increases throughout the length of the 0.75 in. diameter duct, and continues to increase to a few inches beyond duct exit. These results show that an appreciable fraction of the gas exit velocity and temperature is retained throughout the length of the unattached duct as long as the duct diameter is equal to the nozzle diameter.

Figures 5(a) and (b) show total temperature and velocity magnitude, respectively, of the gas for the 12 in. (305 mm) long, 0.75 in. (1.905 mm) diameter duct as a function of distance from the nozzle for Mach numbers from 0.3 to 1.0. The curves for Mach 0.5 are the same as those in Figure 4(a) and (b), except that the temperature axis scale is expanded. Figure 5(a) shows that the gas temperature falls somewhat less for higher Mach number. Figure 5(b) shows that there is a greater drop in velocity at the duct entrance for higher Mach number flow, but the gas velocity recovers nearly to the exit velocity for each case.

Figure 6(a) and (b) shows the absolute gas pressure versus distance from the nozzle exit for the 4 different ducts and for 5 values of the Mach number for the 12 in. (305 mm) duct. For each plot, the pressure begins at the burner pressure appropriate for the particular Mach number of interest. The pressure drops to near atmospheric pressure at the nozzle exit. For the 0.75 in. (19.05 mm) diameter ducts, the pressure rises at the duct entrance and falls back to atmospheric pressure at the duct exit.
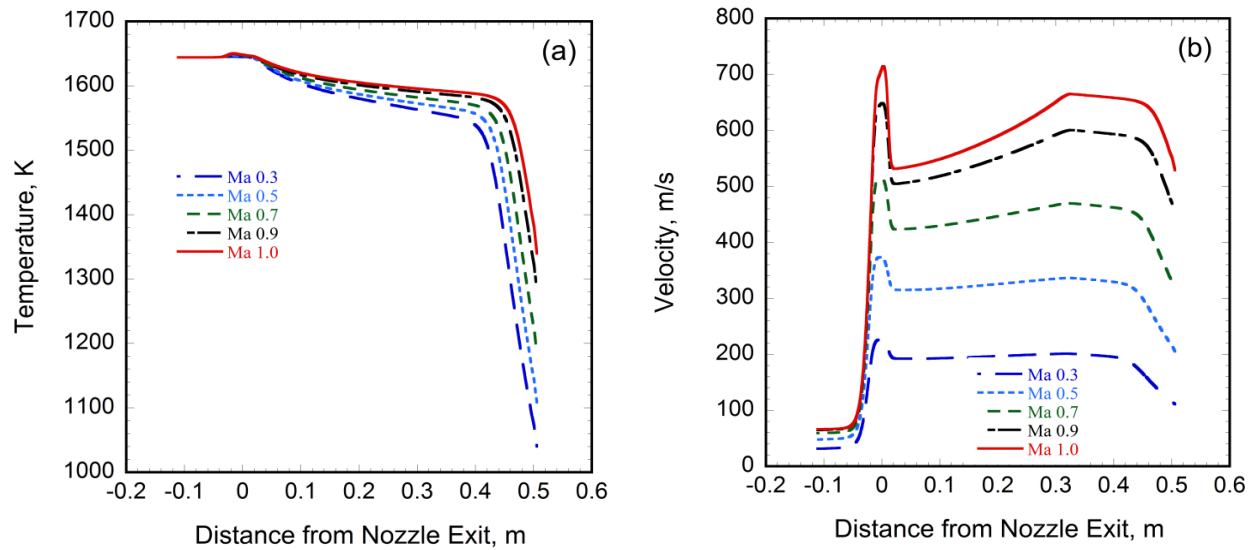
Figure 5.—Plots of gas (a) total temperatures and (b) velocity magnitudes for the 12 in. (305 mm) long, 0.75 in. (19.05 mm) diameter duct as a function of distance from the nozzle exit for Mach numbers from 0.3 to 1.0.
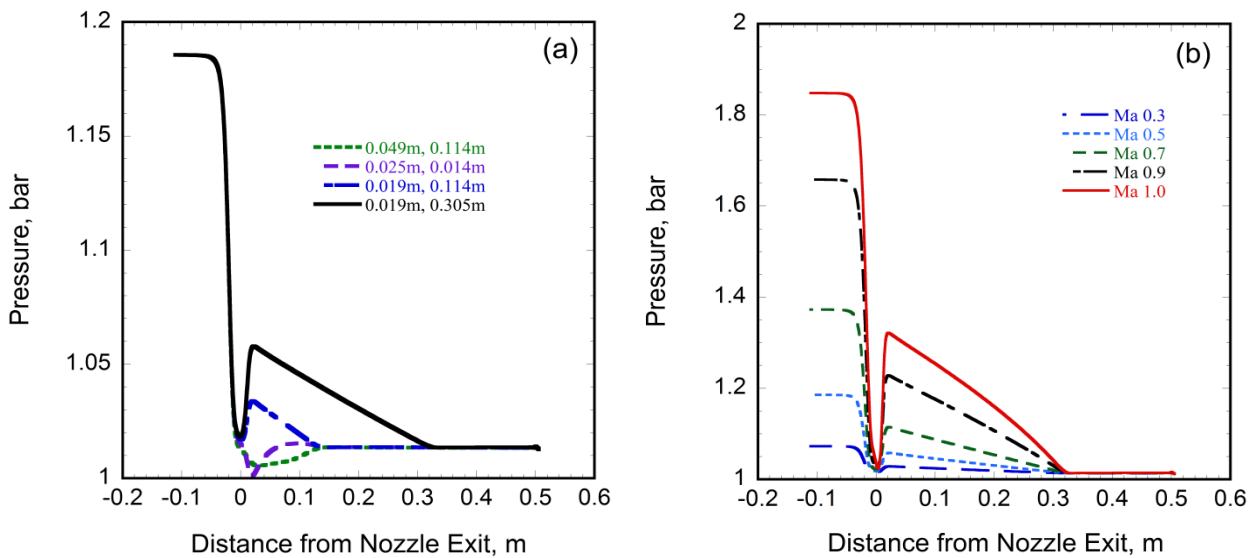

Figure 6.—Absolute gas pressure versus distance from the nozzle exit for (a) the 4 different ducts and (b) for 5 values of the Mach number for the 12 in. (305 mm) long, 0.75 in. (19.05 mm) diameter duct.

Of the large number of particle-track calculations that were made for fine 20 to 32 μm alumina particles, only the 20 m/s injection cases are shown in Figure 7. This conveys the general trends using a more manageable number of figures. Each plot shows the two-dimensional most probable particle tracks on the upper part of the plot and the modeled velocity at the lower part. Note the increase in particle velocity with increasing Mach number. Also note that the velocity drops in half, due to the 0.5 restitution coefficient, whenever the particles strike a wall.
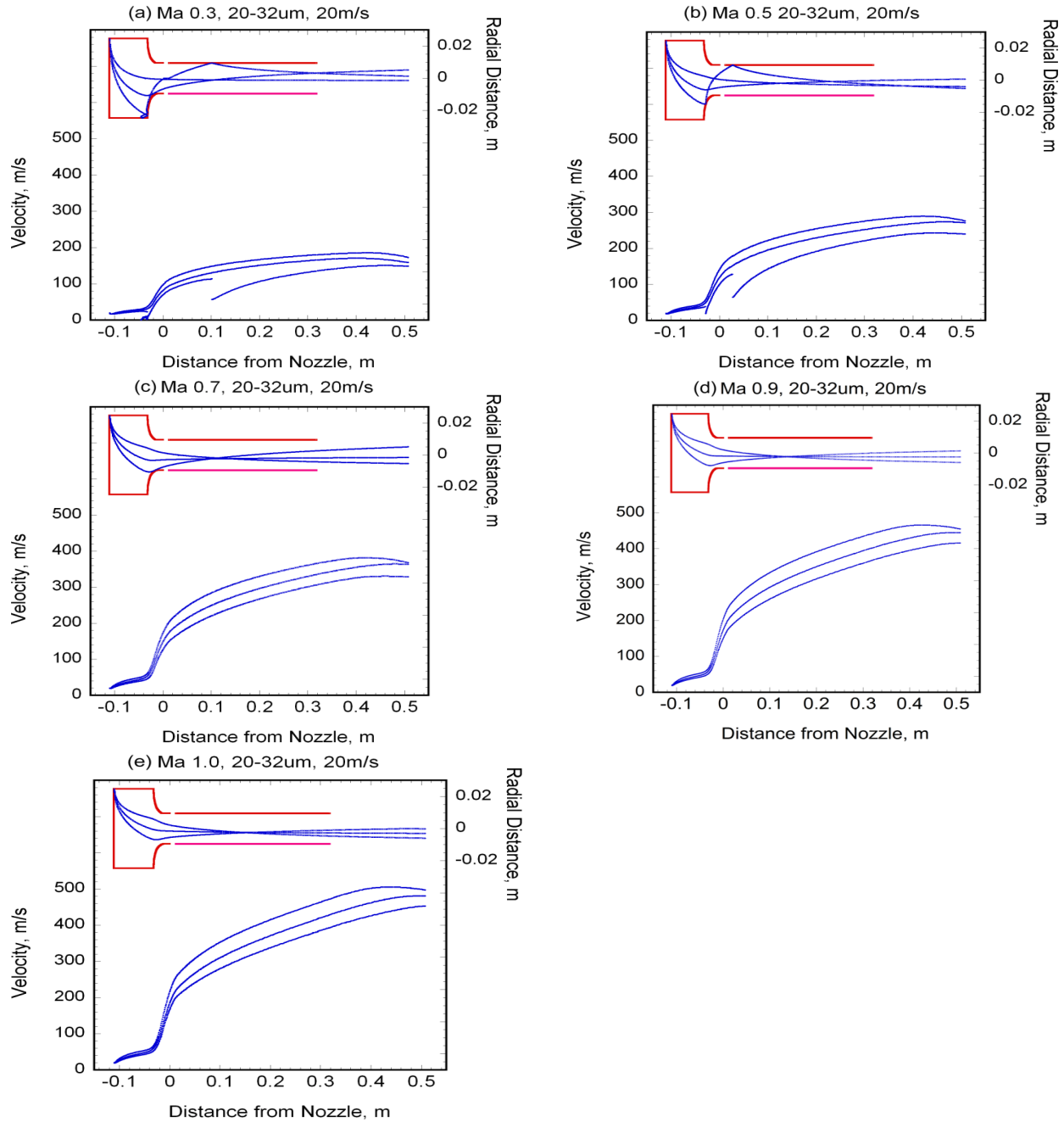
Figure 7.—Most probable particle tracks and velocity magnitudes as a function of distance from the nozzle for 20 to 32 μm alumina particulate fed at 20 m/s into burner rigs operated at Mach numbers from 0.3 to 1.0 for a 12 in. (305 mm) long, 0.75 in. (19.05 mm) diameter duct.
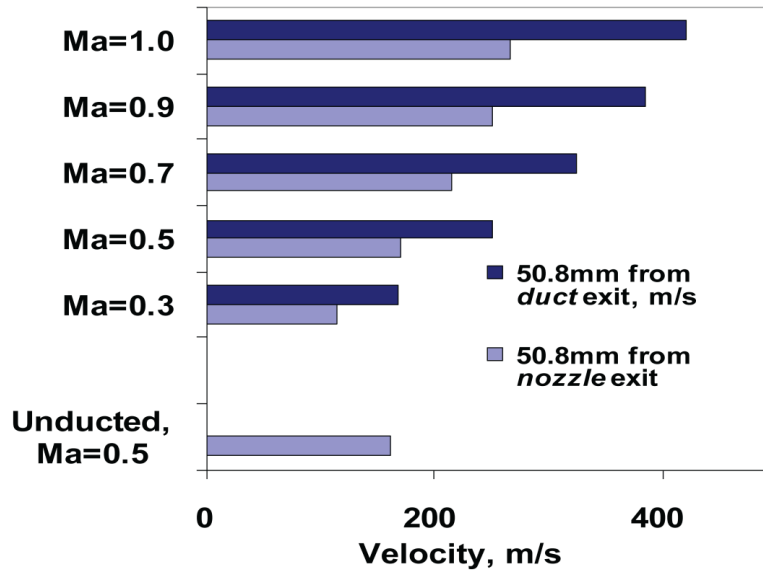
Figure 8.—Median velocity of 20, 26, and 32 μm diameter particulates (26 μm mean diameter) at 2 in. (50.8 mm) from the exit of the nozzle or from the 12 in. (305 mm) duct for Mach numbers ranging from 0.3 to 1.0 for a 12 in. (305 mm) long, 0.75 in. (19.05 mm) diameter.

Because three injection velocities were modeled for each Mach number for the 20-to-32 μm powder, the total number of particle tracks was nine. The velocity attained by each of these tracks is a function of factors such as the particle size, the number and location of wall strikes, and the nearness of the particle tracks to the centerline. In the future, modeling involving a large number of particle tracks accurately replicating a statistical distribution of particle velocities may be conducted. For the current set of calculations, it would be instructive to examine representative particle velocities as a function of Mach number. Among the choices for representative particle velocities is the maximum, mean, or median velocity. Since very high or very low particle velocities will not affect the median value, the median particle velocity was used in Figure 8. Each bar in Figure 8 represents the median of nine velocities (3 injection velocities times 3 particle sizes) at 2.0 in. (50.8 mm) from the duct exit for Mach numbers ranging from 0.3 to 1.0 for the 20 to 32 μm powder (mean particle size 26 μm). The distance of 2.0 in. (50.8 mm) from the duct exit to the specimen was selected as a representative testing distance. The median velocities are plotted in Figure 8, along with the velocity at 2.0 in. (50.8 mm) from the nozzle. This velocity provides an estimate of the velocity that would have been achieved at the specimen if no duct were used. As a check of this assumption, the value at a distance of 2.0 in. (50.8 mm) from the nozzle exit for the 1.94 in. (49.3 mm) diameter duct is plotted on Figure 8 for the Mach 0.5 case. The large diameter 1.94 in. (49.3 mm) duct behaves essentially as an unducted burner rig. Inspection of the figure shows that the median velocity at 2 in. (50.8 mm) from the nozzle is very similar whether the 12 in. (305 mm) duct is present or not. Therefore, the paired bars in the figure may be interpreted as an estimate of the predicted improvement in velocity that these relatively small particles achieved using the unattached duct. The figure shows that the improvement in velocity for these small particles is 47 percent for Mach 0.3, rising to 58 percent for Mach 1.0.

The lower portions of Figure 9(a) through (j) show plots of particle velocity versus distance through the rig for the case of three large diameter particles: 500, 550, and 600 μm. The upper portions of the figures shows the corresponding most probable particle tracks, which are modeled for Mach 0.3 to 1.0. All of the plots shown are for 3 m/s injection, which assumes that the injected particles have been slowed from the faster speed required for conveying through the feed line to a slower speed using, for example, a 45° elbow in the feed line just before injection. Such a device, which will be described later in the report, would prevent possible damage of the burner liner when large particles were used. The plots on the left hand side of the page are calculated assuming a 0.5 restitution coefficient. The plots on the right were for a restitution expression that displayed near-elastic forward scattering (which was especially true for less than 15° incidence). The angle of incidence was allowed to equal the angle of reflectance in all cases. Note that even with the slowed injection velocity, it was not possible to avoid striking the burner liner on the side opposite the injection.
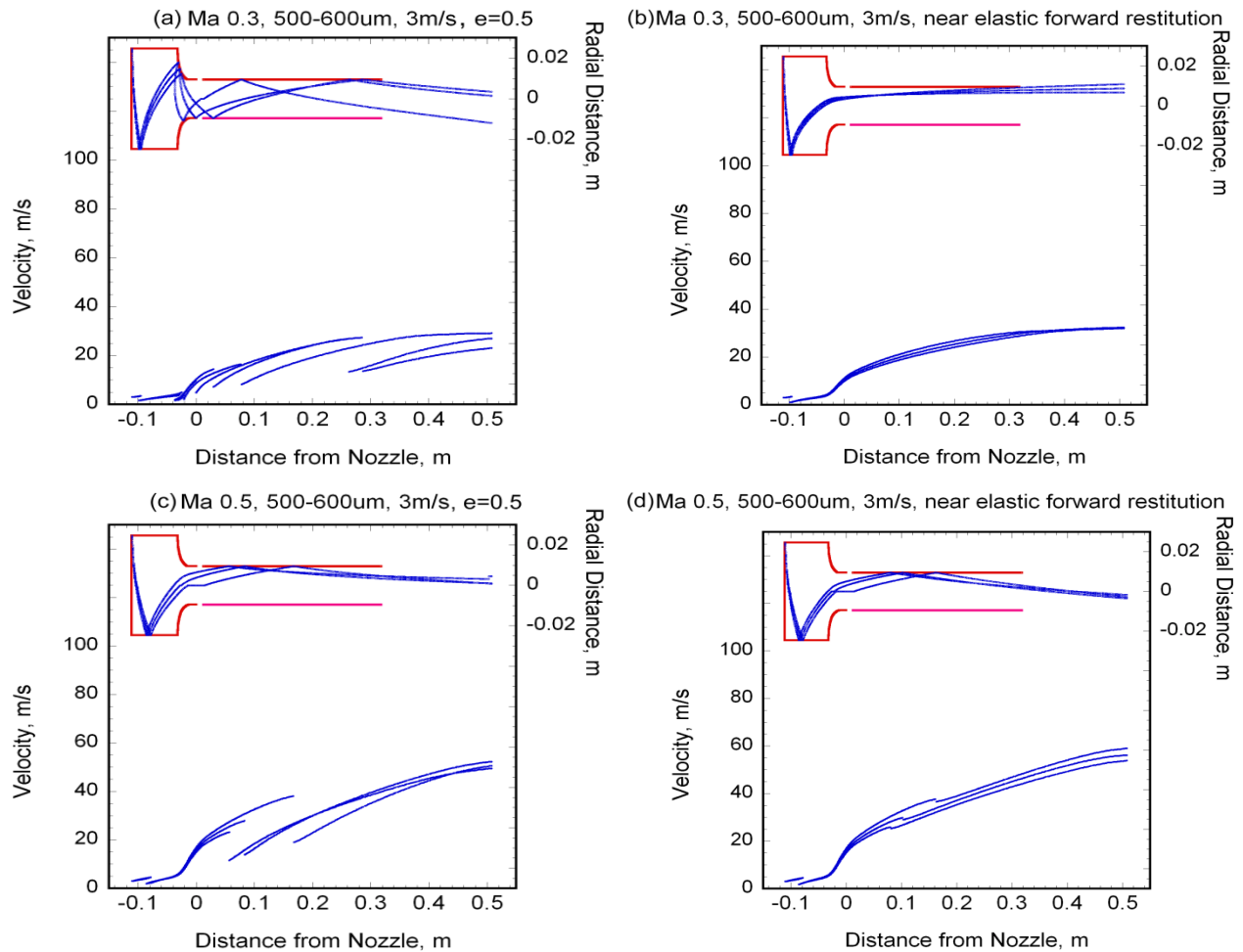

Figure 9.—Most probable particle tracks and velocity magnitudes versus distance from the nozzle for 500, 550, and 600 μm alumina particulate fed at 3 m/s into burner rigs operated at Mach numbers from 0.3 to 0.7; Figures (a),(c) for restitution coefficient, e, of 0.5; Figures (b),(d) for near-elastic forward restitution.
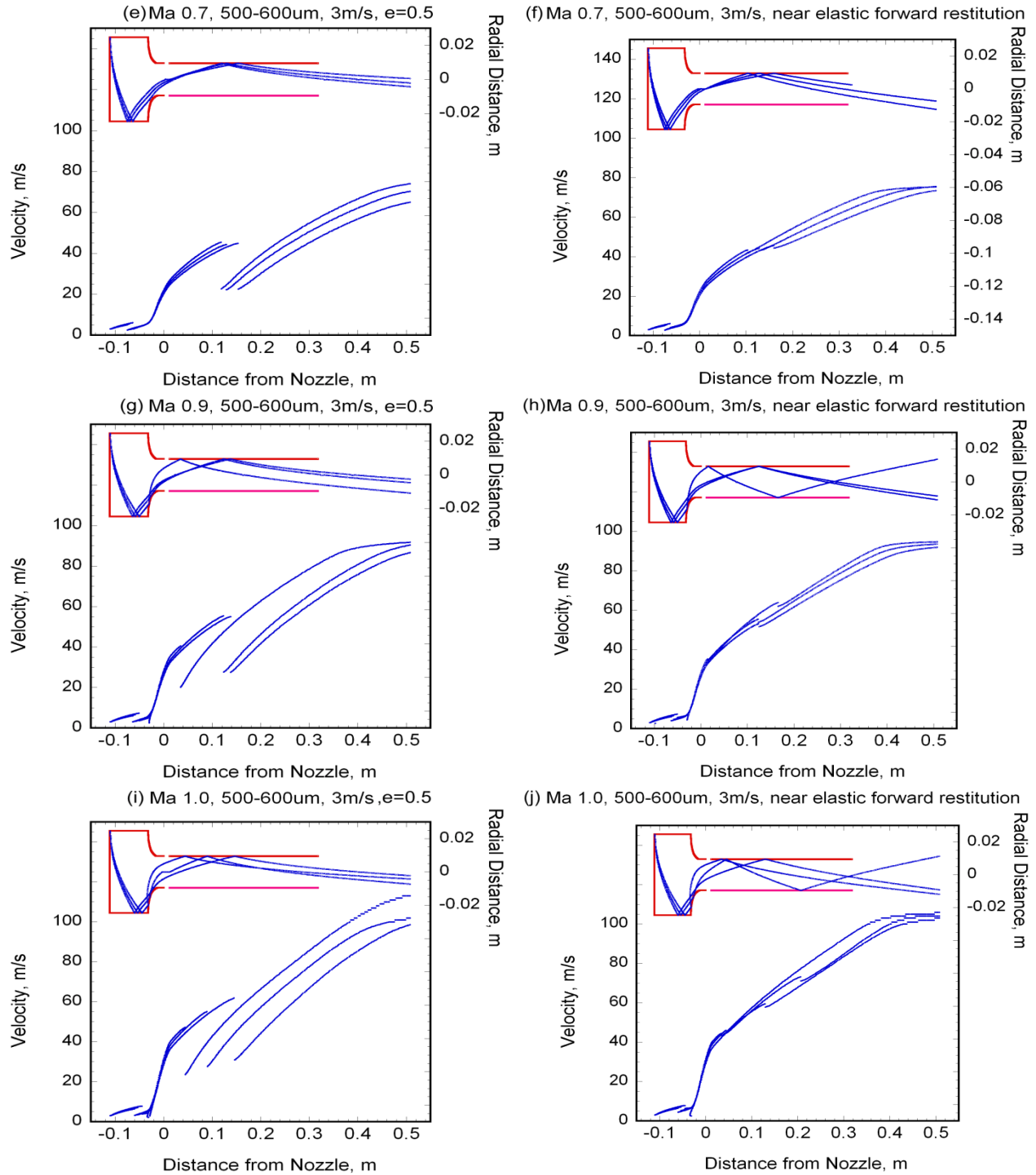
Figure 9.—Concluded. Most probable particle tracks and velocity magnitudes vs. distance from the nozzle for 500, 550, and 600 μm alumina particulate fed at 3 m/s into burner rigs operated at Mach numbers from 0.7 to 1.0; Figures (e),(g),(i) for restitution coefficient, e, of 0.5; Figures (f),(h),(j) for near-elastic forward restitution.

Figure 10 represents the effect of the unattached duct on the velocity of larger 500, 550, and 600 μm diameter particles. As above, the median velocity from a range of injection velocities was plotted at 2.0 in. (50.8 mm) from the nozzle and from the duct exit, respectively. However, for these large particles, this is the middle of only three velocities because only one injection velocity per case was modeled. Also, the results of an unducted case are presented for Mach 0.5 operation. Inspection of the figure shows that the velocity plotted for the unducted case is very similar to the velocity at 2.0 in. (50.8 mm) from the burner nozzle for the ducted cases when compared at the same Mach number. As with the small particles, the ratio of these two velocities is taken to be essentially equal to the enhancement in velocity achievable using the duct. The enhancement was found to be greater for larger Mach numbers and somewhat greater for the cases where near-elastic forward restitution was assumed. Velocity enhancements were found to range from 91 to 114 percent for the near-elastic forward scattering cases. For the cases having the 0.5 restitution coefficient, the velocity enhancement decreased with increasing Mach number from 95 percent at Mach 0.3 to 70 percent at Mach 1.0. For the Mach 0.7 cases, the velocity using the duct was predicted to be increased by 85 or 101 percent, respectively, for the restitution coefficient of 0.5 or the near-elastic forward scattering case. For reference, the enhancement at Mach 0.7 for the small 26 μm particle case was 52 percent.
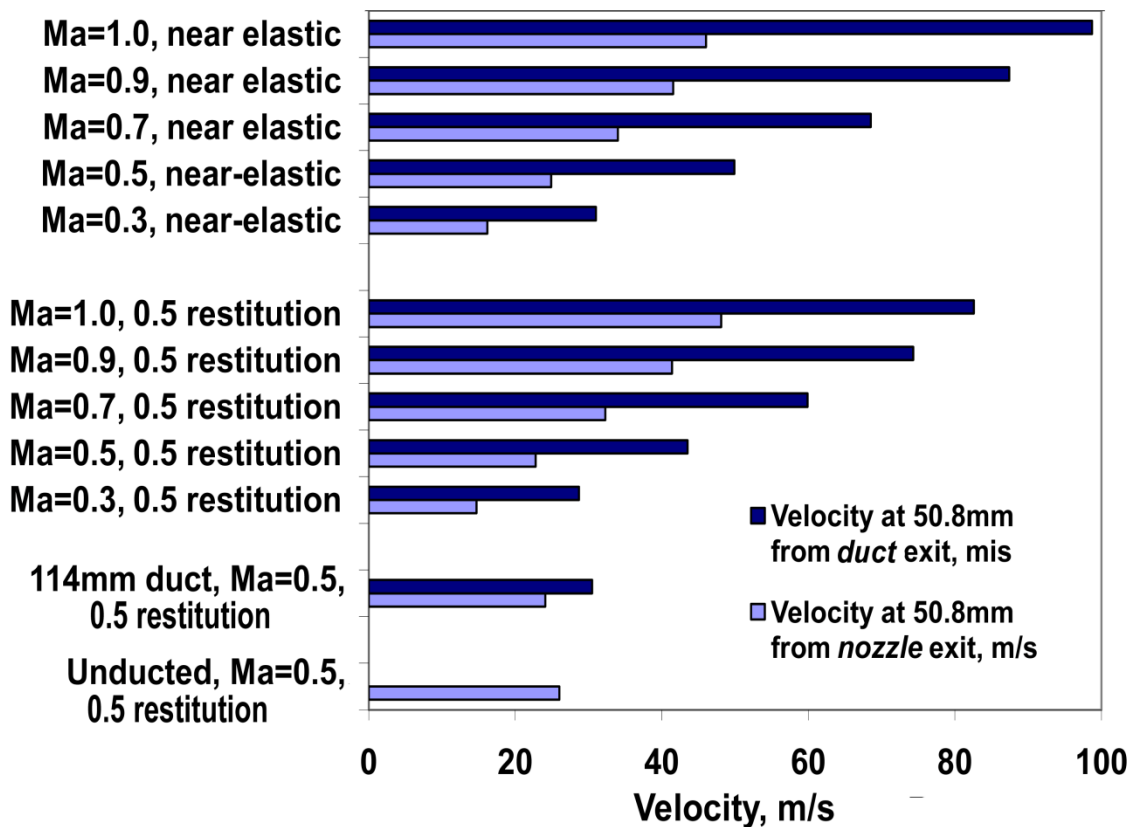

Figure 10.—Median velocity of 500, 500, and 600 μm diameter particulates (550 μm mean diameter) at 2 in. (50.8 mm) from the exit of the nozzle or from the 12 in. (305 mm) duct for Mach numbers from 0.3 to 1.0 for constant 0.5 and near elastic restitution coefficients.

Modeling of Elbow Injector

A related CFD study was conducted to determine whether a device employing a simple 45° elbow fitting followed by a short length of a wider tube could be used to slow down the injection velocity of large particles sufficiently to avoid damage to the burner liner opposite the injection location. For this study, the modeled carrier gas velocity and pressure upstream of the elbow were adjusted so that 500 to 600 μm particles would be conveyed at about 20 m/s. The exit pressure was adjusted to represent the burner pressure for Mach 0.7 burner rig operation. The gas pressure and velocity are shown in Figure 11(a) and (b), respectively. Two different sets of restitution coefficients were employed: in Figure 11(c), constant restitution coefficient of 0.5 and, in Figure 11(d), restitution coefficient near one for angles less than about 15° but falling off at higher angles (i.e., near-elastic forward restitution). Figures representing the results of the modeling are shown below.

From inspection of Figures 11(c) and (d), the injector is shown to slow the particles down considerably for either case. Figures 12(a) and (b) show the velocities of the 12 particle tracks are plotted versus time for the two cases. In these figures, the Y-axis is the velocity in meters per second and the X-axis is the transit time in seconds of the particles. The exit velocity of the particles from injector (which would also be the entrance velocity of the particles into a Mach 0.7 burner) is seen to vary from about 1 to 4 m/s.
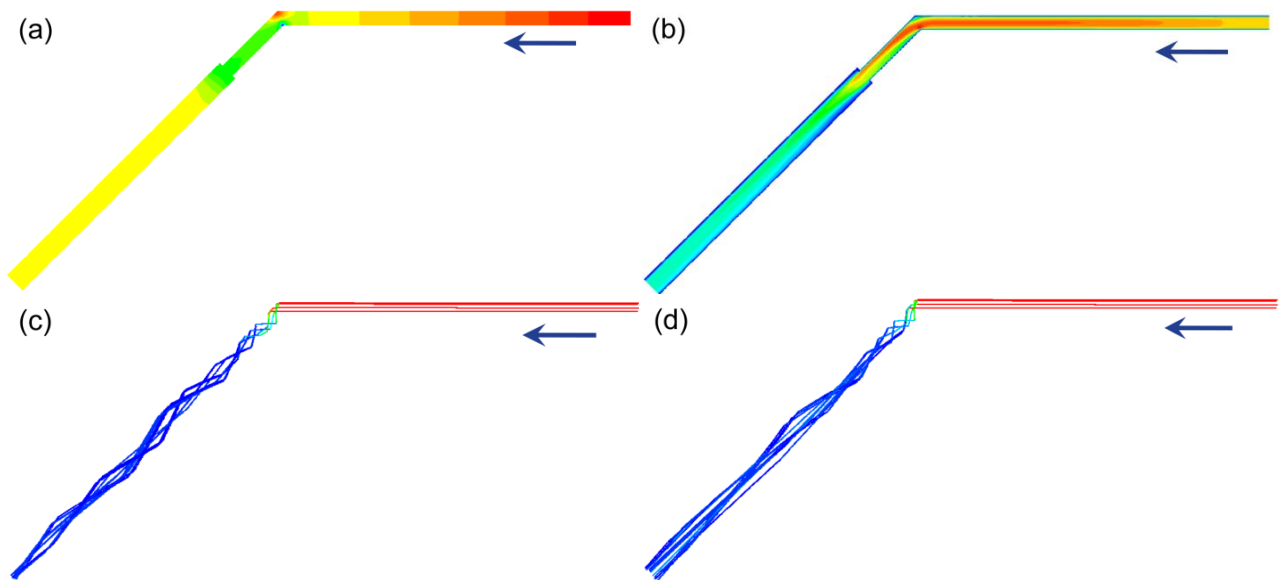

Figure 11.—(a) Gas pressure from 136804 (blue) to 138536 (red) pascals and (b) gas velocity for carrier gas flowing through an elbow injector from 0 (blue) to 44.1 m/s (red), and particle tracks for 12 particles in the range of 500 to 600 μm (550 μm mean) prior to injection into a burner rig operated at Mach 0.7 assuming (c) a restitution coefficient of 0.5 with tracks colored by velocity from 0.45 (blue) to 20.44 (red) m/s and (d) near-elastic forward restitution with tracks colored by velocity from 1.17 (blue) to 20.44 (red) m/s. Arrows refers to the direction of flow.
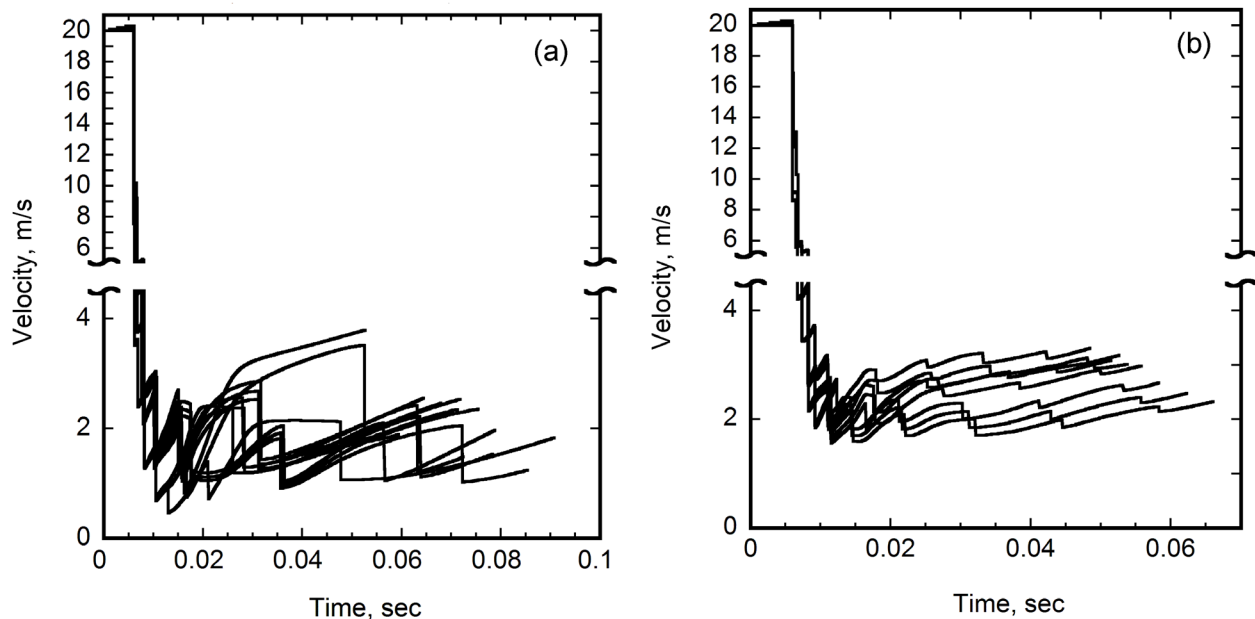
Figure 12.—Particle velocity versus time for 500 to 600 μm (550 μm mean) particles in a 45° elbow injector assuming (a) restitution coefficient of 0.5 or (b) near-elastic forward restitution.

Figure 13.—Photograph of particle injector employing a 45° fitting.

For the assumption of near-elastic forward restitution, shown in the lower set of figures, the exit velocities of the particles are seen to range from a little above 2 m/s to a little above 3 m/s. The particle tracks may be seen to straighten more for the near-elastic case than for the case where the restitution coefficient was assumed to equal a constant value of 0.5. In either case, the particle velocities are slowed to comparable values of generally 2 to 3 m/s. A photograph of an injector employing a 45° fitting constructed from simple fittings is shown in Figure 13. This has been tested and shown to work well.

Experimental Results

An early version of the unattached duct was constructed that had insulation wrapped around the center 10 in. (254 mm) of a 12 in. (305 mm) long, 0.75 in. (19.05 mm) inner diameter, 1.0 in. (25.4 mm) outer diameter mullite tube (Ref. 3). While it initially functioned well from an aerodynamic viewpoint, it suffered from post-test cracking of the mullite tube at the burner end of the duct. A second version, shown in Figures 14(a) and (b), placed the mullite tube inside of a Schedule 40 stainless steel pipe. A specimen temperature of 1800 °F (980 °C) could be achieved, while the temperature of the metal pipe near the nozzle could be kept as low as 1650 °F (900 °C). Ideally, specimen temperatures of 2000 °F (1090 °C) or higher are needed. However, use of this stainless steel pipe prevented testing at temperatures that high. More recently, a Haynes 230 superalloy pipe has been acquired. This alloy is suitable for prolonged use up to 2100 °F (1150 °C) (Ref. 20). Therefore, long duration exposure of specimens to temperatures of 2000 °F or higher is expected to be easily achievable using the superalloy pipe.

A high-speed camera was used to visualize the particle streaks and measure their velocity for both ducted and unducted runs that were conducted in the absence of specimens. Figure 15 for the unducted case, repeated from Reference 3. These images, although necessarily lower resolution that the originals, serve to define the measurement approach. The lines drawn on the figure represent the particle streaks at 1/8000 sec shutter speed of the nominally 27 µm alumina particle size. In Figure 8, the predicted median velocity was 120 m/s at the nozzle exit and 170 m/s at 50.8 mm from the exit. The modeled velocities are quite consistent with the range of experimental velocities shown in Figure 15.
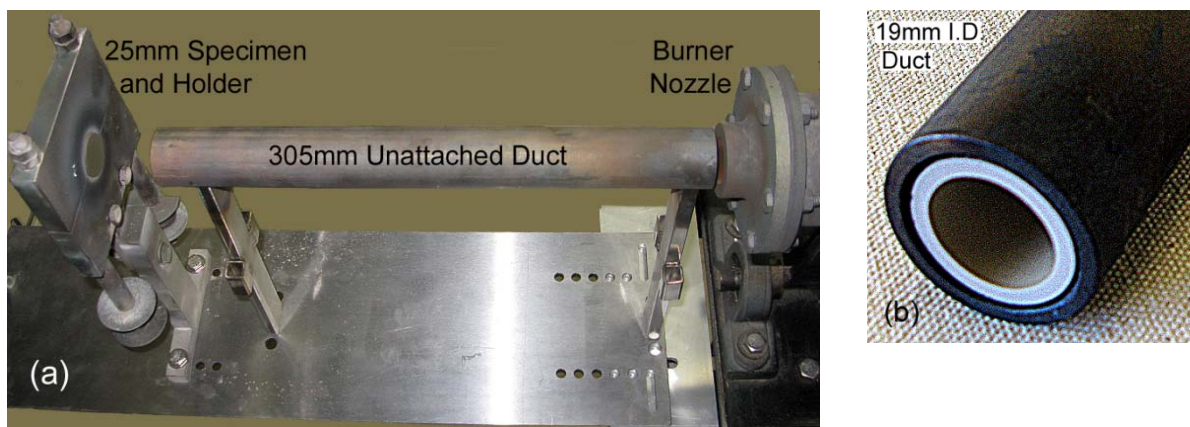

Figure 14(a).—12 in. (305 mm) long, 0.75 (10.05 mm) I.D. duct formed from a ceramic mullite tube within a temporary stainless steel pipe. For later versions, a Haynes 230 superalloy pipe is used; (b) End view of duct.
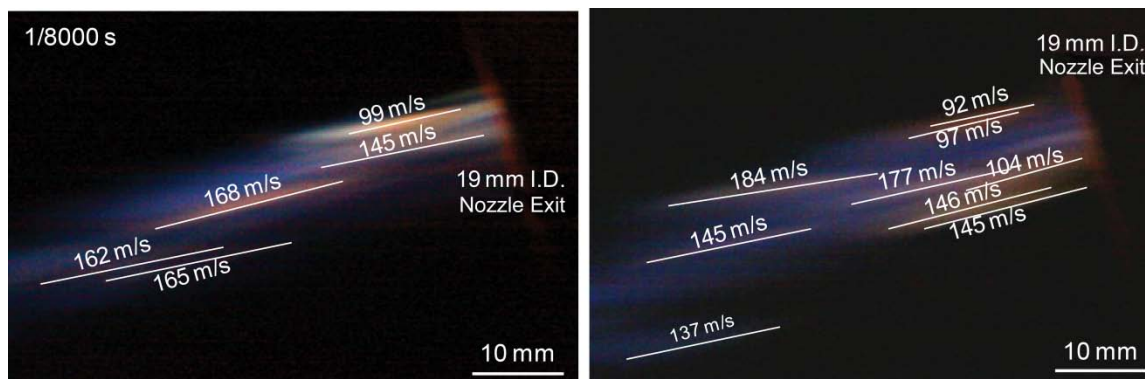

Figure 15.—Tracks of nominally 27 µm particles in the flame exiting from an unducted burner rig operating at Mach 0.5 photographed using 1/8000 sec exposure.

Figure 16 shows particles exiting from the initial ducted rig design. The Mach number for this example was 0.5. The velocity of particles after exiting from the duct was predicted to be about 250 m/s from Figure 8, which is similar to, but somewhat lower than, the velocities of over 300 m/s observed in the streak photograph. This result suggests that the restitution coefficient for small particles within the duct could possibly be higher than the modeled value of 0.5.

Figure 17 shows erosion recession in terms of both thickness and weight loss for a vendor-prepared ZrO_2-7wt%Y_2O_3 baseline EB-PVD TBC on 1 in. (25.4 mm) diameter superalloy specimens, which were eroded in the prototype unattached ducted rig. These were tested using the nominally 27 μm alumina powder at 1800 °F (980 °C) in a Mach 0.5 flame. For the case where recession is expressed in terms of thickness, an error bar representing the 0.0127 mm readability of the micrometer is included on the plot.
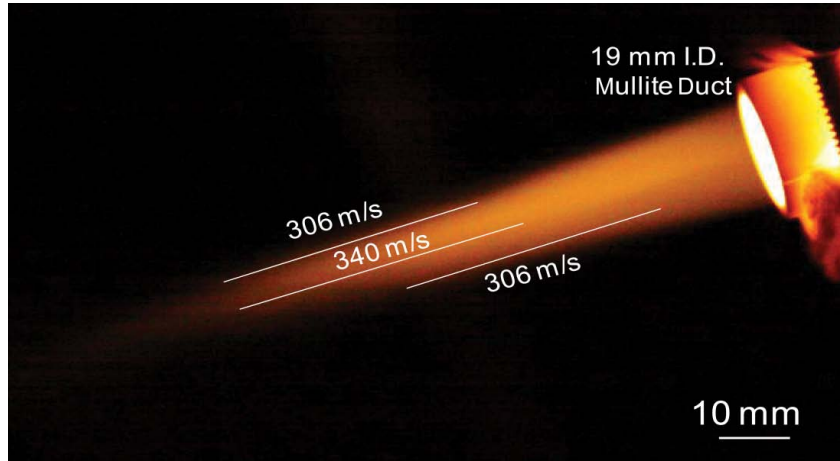

Figure 16.—Tracks of nominally 27 μm particles in the flame exiting from a 12 in. (305 mm) long unattached duct placed in front of a burner rig operating at Mach 0.5 photographed using 1/8000 sec exposure.
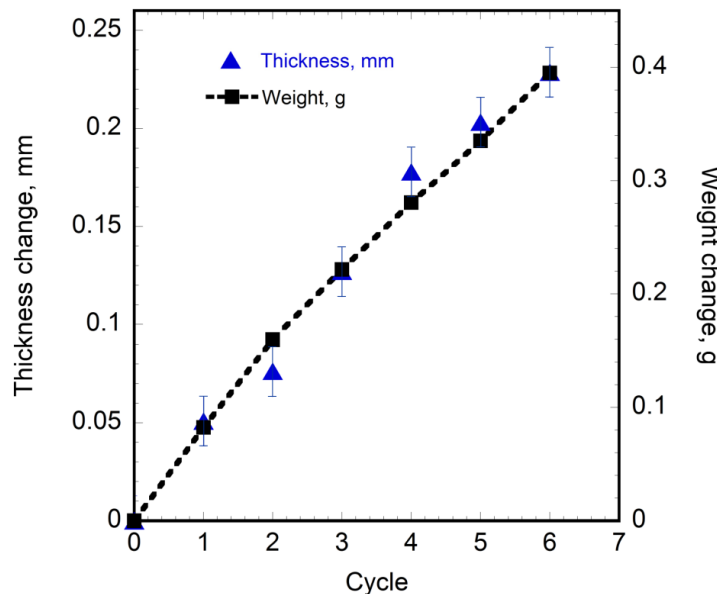

Figure 17.—Recession in terms of thickness and weight loss for a vendor-prepared ZrO_2-7wt%Y_2O_3 baseline EB-PVD TBC on 1 in. (25.4 mm) diameter superalloy specimens eroded in the unattached ducted rig. Tests used the nominally 27 μm powder at 1800 °F (980 °C) using a Mach 0.5 burner rig.

Photos of tested specimens are shown below. Figure 18(a) shows a specimen tested in the unducted rig. Figure 18(b) shows a specimen tested in a ducted rig corresponding to the data in Figure 17. The eroded spot in Figure 18(b) was aligned somewhat below the center of the specimen and it is larger than the eroded spot attained in the unducted test. There are small satellite failures which are believed to be impact in nature from larger particles in the erodent powder. The erosion pattern is much larger than observed from the unducted rig.

Figures 19(a) and (b) are images of the same 1.0 in. (25.4 mm) diameter specimens as in Figure 18(a) and (b). However, the images in Figure 19 were obtained using a contour profiler and processing the data through software written by the first author. These figures show clearly that the specimens are dished from the erosion and that the final 25 µm or so of damage displays a steep uneroded edge that appears to indicate that the final portion of the damage had occurred suddenly.
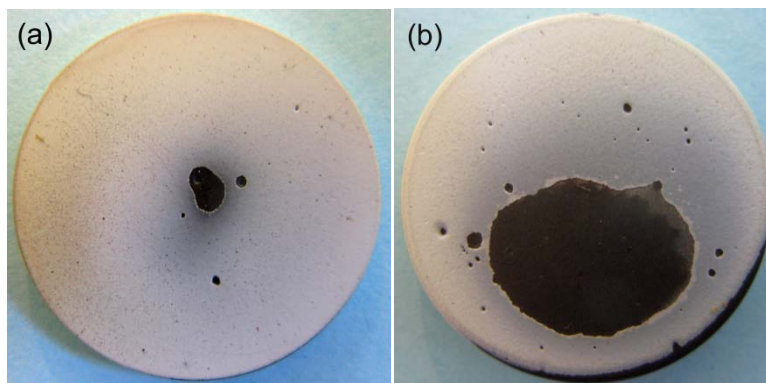

Figure 18.—Photographs of 1.0 in. (25.4 mm) diameter specimens tested in burner rig operated at Mach 0.5; (a) without and (b) with the 12 in. (305 mm) long duct, showing a much larger eroded diameter when the duct was used.
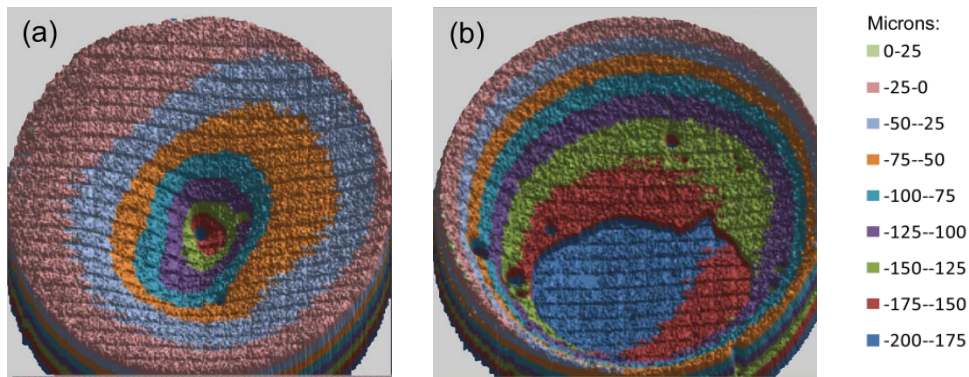

Figure 19.—3D plot of the data obtained from contour profiler of post test specimens tested in burner rig operated at Mach 0.5; (a) without and (b) with the 12 in. (305 mm) long duct, showing a much larger eroded diameter when the duct was used.

Summary and Conclusions

The CFD modeling and experiments discussed in this paper have shown the feasibility of using an unattached duct with a burner rig for increasing injected particle velocity for burner erosion rig exposure of coated specimens as long as the duct has an internal diameter equal to the diameter of the burner rig nozzle. A 12 in. (305 mm) long, 0.75 in. (19.05 mm) diameter duct was found to lead to increased particle velocity, with the velocities of the larger 550 μm particles increasing by a factor of about 1.7 to 2.0 depending on Mach number and restitution coefficient. This compares with a smaller fractional benefit of about 1.5 to 1.6 for the velocities of the smaller 26 μm particles. Another potential benefit of the duct, demonstrated experimentally, is that the particle distribution was observed to spread to a greater diameter at the specimen location when the duct was used, thus increasing the eroded region of the specimen and allowing for more precise determination of average erosion rates. Further experimental work is required to assess the durability of the proposed unattached duct design and to investigate the use of unattached ducts with nozzles having diameters other than the one used in this study.

It has also been shown that an injector made from a simple 45° elbow fitting can be used to slow the particle velocities before injection from the relatively fast velocities needed to convey the powder through the feed line to much slower velocities that are less likely to damage the burner liner.

Appendix.—Analytical Expressions for Particles Having Non-Zero Initial Velocity in a Flowing Gas Stream

The analytical expressions for the velocity of particles in a parallel flowing gas stream may be re-derived to include non-zero initial particle velocity. This will allow examination of the expressions describing the acceleration of particles in a duct after initial acceleration in the burner rig nozzle. Simplifying assumptions include constant gas temperature, velocity, and pressure, as well as spherical particles.

Assuming drag forces predominate, particle dynamics are governed by the following expression (Ref. 21)

$$m\frac{dV_p}{dT} = mV_p\frac{dV_p}{dx} = C_d\, A_p\, \frac{\rho}{2}\left(V - V_p\right)\left|V - V_p\right| \tag{2}$$

where the parameters referring to the particle are mass m, velocity V_p, and cross sectional area A_p. The gas parameters are velocity V, which is assumed to be constant, and density ρ; C_d is the drag coefficient.

The above expression may be rearranged to give

$$dx = \frac{2\,m}{c_d\, A_p\, \rho}\frac{V_p\, dV_p}{\left(V - V_p\right)\left|V - V_p\right|} \tag{3}$$

For spheres of diameter D and density ρ_p:

$$m = \frac{\pi}{6}D^3\rho_p \tag{4}$$

$$A_p = \frac{\pi}{4}D^2 \tag{5}$$

Therefore, we may write:

$$dx = \frac{4}{3}\frac{D}{C_d}\frac{\rho_p}{\rho}\frac{V_p\, dV_p}{\left(V - V_p\right)\left|V - V_p\right|} \tag{6}$$

For the greatly simplifying assumption of constant C_d and with accelerating particles:

$$\int_{x_i}^{x_f} dx = \frac{4}{3}\frac{D}{C_d}\frac{\rho_p}{\rho}\int_{V_i}^{V}\frac{V_p\, dV_p}{\left(V - V_p\right)\left|V - V_p\right|} \tag{7}$$

$$x_f - x_i = \frac{4}{3}\frac{D}{C_d}\frac{\rho_p}{\rho}\left[\ln\frac{V - V_p}{V - V_i} + \frac{V}{V - V_p} - \frac{V}{V - V_i}\right] \tag{8}$$

The above expression is the same as the expression in the literature, except that the literature equation was derived for zero initial velocity. If the initial particle velocity V_i is set to zero, the equation for the literature is obtained. In our case, the initial velocity may represent the velocity of the particle as it exits the nozzle.

A somewhat less simplifying assumption of C_d proportional to the square root of the Reynolds number can also lead to an equation for particle velocity versus distance that may be integrated in closed form. The simplified square-root drag law is:

$$C_d = B\,Re^{1/2} \tag{9}$$

$$Re = \rho D |V - V_p| / \mu \tag{10}$$

where μ is the dynamic viscosity of the gas, and B is an arbitrary constant. This leads to the following expressions:

$$x_f - x_i = \frac{4}{3}\frac{\rho_p}{\rho}\left(\frac{\mu D}{\rho}\right)^{1/2} B \int_{V_i}^{V} \frac{V_p\,dV_p}{\left(V - V_p\right)^{3/2}} \tag{11}$$

$$x_f - x_i = \frac{4}{3}\frac{\rho_p}{\rho^{3/2}}(\mu D)^{1/2} B \left[\frac{V}{\left(V - V_p\right)^{1/2}} - \left(V - V_p\right)^{1/2} - \frac{V}{\left(V - V_i\right)^{1/2}} - \left(V - V_i\right)^{1/2}\right] \tag{12}$$

The above equation is useful for visualizing the approximate influence of the various parameters. It may also be used to check closed-form solutions to solutions from numerical integration where the constant B can be selected to give the best match in the range of interest of the Reynolds number to the drag coefficient calculated using a more accurate drag law. For a more accurate drag law, such as the Abraham equation (Ref. 22) that is sufficiently accurate for Re <5000, an expression may be obtained that must be numerically integrated. The Abraham equation is:

$$C_d = 0.2924\left[1 + \frac{9.06}{Re^{1/2}}\right]^2 = 0.2924 + \frac{5.291}{Re^{1/2}} + \frac{24.00}{Re} \tag{13}$$

The expanded version clearly shows that C_d goes from the Stoke's Law equation (24/Re) for very small Re towards 0.2924 for very large Re (at Re = 5000, C_d = 0.2972). This leads to the following expression that must be integrated numerically:

$$\int_{x_i}^{x_f} dx = \frac{4}{3}D\frac{\rho_p}{\rho}\int_{V_i}^{V}\frac{V_p\,dV_p}{Cd\left(V - V_p\right)|V - V_p|} \tag{14}$$

$$x_f - x_i = \frac{4}{3}D\frac{\rho_p}{\rho}\int_{V_i}^{V}\frac{V_p\,dV_p}{0.2924\left[1 + \dfrac{9.06}{Re^{1/2}}\right]^2 \left(V - V_p\right)|V - V_p|} \tag{15}$$

The Abraham equation covers the entire range of Reynolds numbers of interest to this study. However, the CFD code FLUENT used the Morsi and Alexander equation (Ref. 17), as discussed in the Model Description section. The expanded version of the Abraham drag law is similar in form to the equation of Morsi and Alexander. However, with the Morsi and Alexander equation, the $Re^{1/2}$ term is replaced by Re and the Re term is replaced by Re^2. The constant terms for the Abraham and the Morsi and Alexander equations are different from each other. In fact, the Morsi and Alexander equation uses different constants for different ranges of the Reynolds number, which allows either equation to predict similar values of C_d. This leads to the following relationship between particle velocity and distance:

$$x_f - x_i = \frac{4}{3} D \frac{\rho_p}{\rho} \int_{V_i}^{V} \frac{V_p dV_p}{\left[a_1 + a_2 / \text{Re} + a_3 / (\text{Re})^2 \right] \left(V - V_p \right) \left| V - V_p \right|}$$

(16)

The above analytical expression, which uses the same drag law that is used for the CFD analysis, may be numerically integrated to obtain estimates of the particle velocity versus distance from the nozzle exit. During the numerical integration, care must be taken to use the constants in the Morsi and Alexander equation that are appropriate for the Reynolds number range of interest. An example of the results of such a numerical integration is shown in Figure 20, where curves for 26 and 550 µm particles being accelerated under Mach 0.5 conditions are plotted, along with the corresponding results from the CFD analyses, which had previously been presented in Figures 7 and 9. Mean values of the gas temperature, pressure and velocity (1573K, 1.034 MPa, and 310 m/s, respectively), that are needed for the analytical expression, were taken from the CFD calculations. Even with the simplification of using mean values for these gas properties, the results from the analytical expression matches the CFD modeled results very well. For the 550 µm case, the velocities drop somewhat beyond approximately 0.1 m because the particles strike the duct wall. The analytical expression initially matches very well, but after the wall strike the analytical expression somewhat over predicts because the analytical expression cannot account for the drop in velocity due to a wall strike.
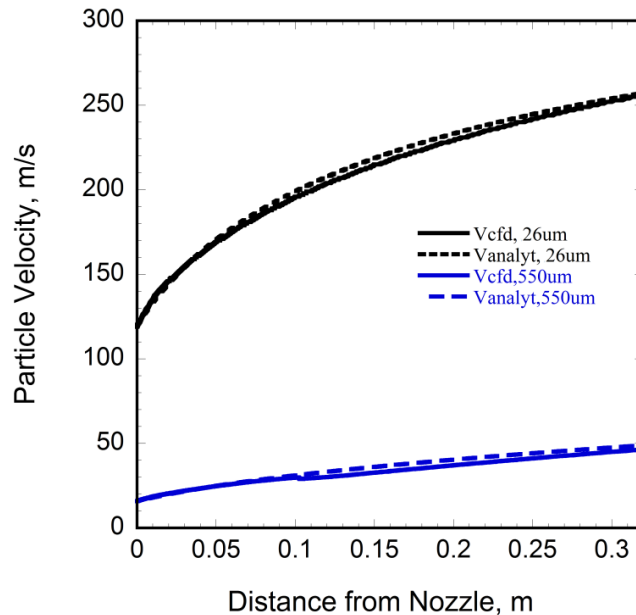

Figure 20.—Predicted velocities of 26 and 550 µm particles for the ducted Mach 0.5 case as predicted by the CFD analysis and by the analytical expression. The CFD analysis is used to provide the initial particle velocity (i.e., the particle velocity and the nozzle exit) and the mean values of the gas velocity, temperature, and pressure.

References

1. Yamamuchi, G.K., and L.A. Young, *A Status of NASA Rotorcraft Research*. NASA Technical Paper NASA/TP—2009-215369; Sept 2009.
2. Dongming Zhu and Robert A. Miller; *Development of Advanced Low Conductivity Thermal Barrier Coatings*. Int. Journal of Applied Ceram Technol, 2005, 1(1): pp. 86–94.
3. Zhu, D., R.A. Miller, and M.A. Kuczmarski. Development and Life Prediction of Erosion Resistant Turbine Low Conductivity Thermal Barrier Coatings NASA/TM—2010-215669; Feb 2010.
4. Wellman, R.G., M.J. Deakin, and J.R. Nicholls, *The effect of TBC morphology on the erosion rate of EB PVD TBCs,* Wear, 2005. 258: pp. 349–356.
5. Borom, M.P., C.A. Johnson, and L.A. Peluso, *Role of environmental deposits and operating surface temperature in spallation of air plasma sprayed thermal barrier coatings*, Surf Coatings Technol., 1996. 86–87: pp. 116–126.
6. Roberts, G.D., R.T. Bhatt, P.J. Bonacuse, R.G. Bryant, M.C. Halbig, K.E. Jackson, W.C. Jackson, J.C. Johnston, M.A. Kuczmarski, R.A. Miller, T.K. O'Brien , *Chapter 8, Structures and Materials* in G.K. Yamamuchi and L.A. Young*, A Status of NASA Rotorcraft Research*. NASA Technical Paper NASA/TP—2009-215369; Sept 2009, pp. 325–376.
7. Hamed, A., Y.D. Jun, and J.J. Yeuan, *Particle dynamics simulations in inlet separator with an experimentally based bounce model*, J Propulsion Power, 1995. 11(2): pp. 230–235.
8. Zedan, M., P. Hartman, A. Mostafa, A. Sehra, *Viscous flow analysis for advanced inlet particle separators,* AIAA-90-2136 (1990).
9. Strangman, T.E., D. Narasimhan, J.P. Armstrong, K.R. Karesek, *Carbon Deposit Inhibiting Thermal Barrier Coating for Combustors*, Patent No. US 6.656,600 B2, Dec 2, 2003.
10. Mariocchi, A., A. Bartz, and D. Wortman, *PVD Experience on GE Aircraft Engines*, J Thermal Spray Technology, (1997). 6(2): pp. 193–198.
11. Bruce, R.W., "Development of 1232 °C (2250 °F), *Erosion and Impact Tests for Thermal Barrier Coatings*, Tribology Transactions, (1998). 41(4): pp. 399–410.
12. Handschuh, R.F., *High Temperature Erosion of Plasma-Sprayed Yttria-Stabilized Zirconia in a Simulated Turbine Environment*, NASA TP 2406; AVSCOM TR-84-C-17, December 1984. Also AIAA–85–1219.
13. Hamed, A.A., W. Tabakoff, R.B. Rivir, K. Das, P. Arora, *Turbine blade surface deterioration by erosion*, J. Turbomachinery, (2005). 127: pp. 445–452.
14. Hamed, A., W. Tabakoff, and R. Wenglarz, *Erosion and Deposition in Turbomachinery,* J Prop Power, (2006). 22(2): pp. 350–360.
15. ANSI/ASME MFC-3M-2004, *Measurement of Fluid Flow in Pipes Using Orifice, Nozzle, and Venturi, Includes Addenda A*, American Society of Mechanical Engineers / 01-Jan-2004 / 92 pages.
16. Senesh, K., and V. Babu, *Numerical Simulation of Subsonic and Supersonic Jets,* 11th AIAA/CEAS Aeroacoustics Conference (26th AIAA Aeroacoustics Conference) 23–25 May 2005, Monterey, California AIAA–2005–3095.
17. Morsi S.A. and A.J. Alexander, *An Investigation of Particle Trajectories in Two-Phase Flow Systems*, J. Fluid Mech., (1972). 55: pp. 193–208.
18. Clift, R., J. Grace, J.R. and M.E. Weber. *Bubbles, Drops, and Particles*, 1978, Academic Press, p. 276. (Dover Pub Inc. 2005 reproduction).
19. Swar, R., *Particle Erosion of Gas Turbine Thermal Barrier Coatings*; A thesis submitted to the University of Cincinnati in partial fulfillment of the requirements for the degree of Master of Science (M.S.) in the Department of Aerospace Engineering and Engineering Mechanics of the College of Engineering, 2009.

20. Haynes International, High temperature Tech Brief, Hanes® 230® Alloy, H-3024E, Haynes International Inc. 2009.
21. Dykhuizen, R.C., and M.F. Smith, *Gas Dynamic Principles of Cold Spray*, J Thermal Spray Technol., 1998. 7(2): pp. 205–212.
22. Abraham, F.F., *Functional dependence of drag coefficient of a sphere on Reynolds number*. Phys. Fluids, 1970. 13: pp. 2194–2195.

1. REPORT DATE (DD-MM-YYYY) 01-06-2011	2. REPORT TYPE Technical Memorandum	3. DATES COVERED (From - To)

4. TITLE AND SUBTITLE Burner Rig With an Unattached Duct for Evaluating the Erosion Resistance of Thermal Barrier Coatings		5a. CONTRACT NUMBER
		5b. GRANT NUMBER
		5c. PROGRAM ELEMENT NUMBER
6. AUTHOR(S) Miller, Robert, A.; Kuczmarski, Maria, A.; Zhu, Dongming		5d. PROJECT NUMBER
		5e. TASK NUMBER
		5f. WORK UNIT NUMBER WBS 877868.02.07.03.05.01.02

7. PERFORMING ORGANIZATION NAME(S) AND ADDRESS(ES) National Aeronautics and Space Administration John H. Glenn Research Center at Lewis Field Cleveland, Ohio 44135-3191	8. PERFORMING ORGANIZATION REPORT NUMBER E-17671

9. SPONSORING/MONITORING AGENCY NAME(S) AND ADDRESS(ES) National Aeronautics and Space Administration Washington, DC 20546-0001	10. SPONSORING/MONITOR'S ACRONYM(S) NASA
	11. SPONSORING/MONITORING REPORT NUMBER NASA/TM-2011-217008

12. DISTRIBUTION/AVAILABILITY STATEMENT
Unclassified-Unlimited
Subject Categories: 27 and 34
Available electronically at http://www.sti.nasa.gov
This publication is available from the NASA Center for AeroSpace Information, 443-757-5802

13. SUPPLEMENTARY NOTES

14. ABSTRACT
Extensive computational fluid dynamics (CFD) modeling backed by experimental observation has demonstrated the feasibility of using an unattached duct to increase the velocity and spatial spread of erodent particles exiting from a burner rig. It was shown that gas velocity and temperature are mostly retained if the inner diameter of the unattached duct equaled the exit diameter of the burner rig nozzle. For particles having a mean diameter of 550 mm, the modeled velocity attained at a distance 2.0 in. (50.8 mm) beyond the exit of a 12 in. (305 mm) long duct was approximately twice as large as the velocity the same distance from the nozzle when the duct was not present. For finer particles, the relative enhancement was somewhat less-approximately 1.5 times greater. CFD modeling was also used to guide the construction of a device for slowing down the velocity of the particles being injected into the burner rig. This device used a simple 45° fitting to slow the particle velocity in the feed line from 20 m/s, which is in the range needed to convey the particles, to about 3 m/s just as they are injected into the burner. This lower injection velocity would lessen the severity of the collision of large particles with the wall of the burner liner opposite the injection port, thereby reducing potential damage to the burner liner by high-velocity particles.

15. SUBJECT TERMS
Computational fluid dynamics (CFD); Erosion; Thermal control coatings

16. SECURITY CLASSIFICATION OF:			17. LIMITATION OF ABSTRACT	18. NUMBER OF PAGES	19a. NAME OF RESPONSIBLE PERSON STI Help Desk (email:help@sti.nasa.gov)
a. REPORT U	b. ABSTRACT U	c. THIS PAGE U	UU	30	19b. TELEPHONE NUMBER (include area code) 443-757-5802